

---

# Efficient Multi Subject Visual Reconstruction from fMRI Using Aligned Representations

---

Christos Zangos<sup>\*1</sup> Danish Ebadulla<sup>\*1</sup> Thomas Sprague<sup>2</sup> Ambuj Singh<sup>1</sup>

## Abstract

This work introduces a novel approach to fMRI-based visual image reconstruction using a subject-agnostic common representation space. We show that the brain signals of the subjects can be aligned in this common space during training to form a semantically aligned common brain. This is leveraged to demonstrate that aligning subject-specific lightweight modules to a reference subject is significantly more efficient than traditional end-to-end training methods. Our approach excels in low-data scenarios. We evaluate our methods on different datasets, demonstrating that the common space is subject and dataset agnostic.

## 1. Introduction

Over the past several decades, the use of machine learning techniques has enabled decoding and/or reconstruction of information represented in neural activation patterns measured in awake, behaving humans. Because the neural representations supporting behavior likely entail patterns of activity across large swaths of tissue, these approaches are thought to offer a key step towards characterizing and quantifying the computational principles brains use to support cognition (Naselaris et al., 2011).

Early approaches, including self-supervised learning frameworks (Beliy et al., 2019; Gaziv et al., 2022; Mozafari et al., 2020; Shen et al., 2019; Seeliger et al., 2018; Ren et al., 2021) struggled to generate semantically accurate image reconstructions, often resulting in images with limited resemblance to the original stimuli. Furthermore, these methods required large amounts of data for training, and their generalization to a wider population of subjects was severely limited. Significant advancements were achieved by incorporating multimodal data, such as text (Lin et al., 2022),

and later by leveraging the generative power of latent diffusion models (LDMs) (Takagi & Nishimoto, 2023; Scotti et al., 2023; Lu et al., 2023; Xia et al., 2024). These models introduced novel mapping techniques to project fMRI signals into the input space of LDMs, yielding higher-quality natural images. However, despite the improved fidelity, the issue of generalization to new participants persisted. In response, (Scotti et al., 2024) proposed projecting fMRI data into a shared representation space, demonstrating significant improvements in both performance and generalizability.

Beyond being able to use decoding and reconstruction approaches to provide evidence of the existence of information represented in a particular brain activation pattern, an additional goal is to compare decoding or reconstruction performance across experimental manipulations, such as cued visual attention (Serences & Boynton, 2007; Kamitani & Tong, 2005; Scolaro et al., 2012; Sprague & Serences, 2013; Itthipuripat et al., 2019; Sprague et al., 2018) and visual working memory (Serences et al., 2009; Harrison & Tong, 2009; Ester et al., 2013; Sprague et al., 2014; Christophel et al., 2012; Li et al., 2021). However, for these approaches to be useful for a cognitive neuroscience lab, the lab would need to acquire sufficient data to train a decoding or reconstruction model for each individual participant (often >20 per study to attain statistical power). The state-of-the-art methods described above use extremely massive datasets with dozens of hours of fMRI data per participant, which is not feasible in almost all cases. Thus, there is a clear need to maximize the efficiency and generalizability of image reconstruction methods such that a model for a new participant can be trained using as little data as possible.

In this work, we introduce an efficient and generalizable approach to fMRI-based visual reconstruction that leverages a subject-agnostic common representation space. Unlike previous approaches that perform end-to-end training of fMRI signals to mapped contextual embeddings, we propose aligning brain activity from new subjects to a pre-trained reference subject in a shared representation space using Adapter Alignment (AA) training. Throughout this work, we refer to lightweight subject-specific modules designed to map input fMRI signals to a shared representation space as "adapters" (Liu et al., 2024). These modules are im-

---

<sup>\*</sup>Equal contribution <sup>1</sup>Department of Computer Science, University of California, Santa Barbara, USA <sup>2</sup>Department of Psychological and Brain Sciences, University of California, Santa Barbara, USA. Correspondence to: Christos Zangos <christoszangos@ucsb.edu>.

plemented as single-layer neural networks. In their linear form, adapters consist of a single linear transformation layer, while in the non-linear form, they include a linear layer followed by a non-linear activation function such as GELU (Hendrycks & Gimpel, 2023). Using AA training, we significantly reduce the amount of fMRI data required and the training time necessary to achieve accurate reconstructions and improve the reconstruction quality. Our method achieves better performance than the training method used by existing state-of-the-art models, but with far fewer training hours, making it feasible for cognitive neuroscience labs with limited data collection resources. We build on this approach by also proposing an adaptive image selection strategy, allowing for optimal fine-tuning of new subjects with minimal data, further improving the practicality and accessibility of fMRI-based image reconstruction. Finally, we evaluate our proposed methods on different datasets.

Our contributions to this work are as follows:

- We provide strong evidence for the existence of a common visual representation space across subjects, where brain activity from different individuals can be aligned in a shared space. By extracting and analyzing embeddings from a pre-trained model, we show that even without explicit alignment, subject-specific fMRI signals, when mapped to a common space display similar behavior and representation structures. Furthermore, we demonstrate that applying a simple orthogonal transformation improves the alignment of embeddings between subjects, and using non-linear adapters with explicit mapping leads to almost perfect alignment across subjects in the common space. (Section 2)
- We introduce Adapter Alignment (AA), a novel approach to facilitate efficient subject-specific alignment in fMRI-based visual reconstruction. Our training pipeline first pre-trains on a reference subject, then aligns new subjects' brain data using lightweight adapters that map them to the shared common space. This process, which is more efficient than traditional end-to-end training, enables faster convergence and better performance, particularly in low-data scenarios. By incorporating MSE losses at the adapter level for common images, we show that our method not only reduces training time but also improves generalization and reconstruction quality. We also present scaling experiments to show that AA training is scalable and agnostic to the components used in the pipeline. (Section 3, Appendix Section A)
- We develop a greedy image selection algorithm that identifies the most representative subset of images for training new subjects. By efficiently selecting fMRI signals that capture the most informative aspects of the

common space, this strategy significantly reduces the amount of data required for fine-tuning without sacrificing performance (from a baseline of 250 images to 150 images). This makes our method more practical for real-world applications, where acquiring large fMRI datasets is often prohibitively expensive. (Section 4)

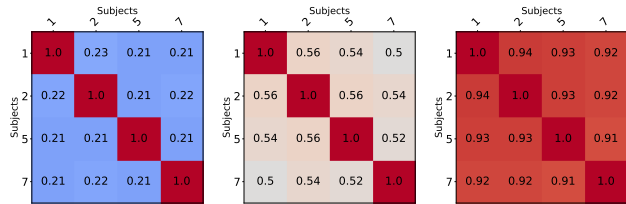
- We validate the generalizability of our approach by applying it to data acquired from different MRI scanners. In particular, we leverage the THINGS dataset (Hebart et al., 2023) to fine-tune our pre-trained models, originally trained on the NSD dataset. Despite the variations in scanning protocols and data characteristics, our Adaptive Alignment (AA) strategy continues to outperform conventional fine-tuning. (Section 5)

## 2. A Common Visual Representation Space

Central to our approach is the hypothesis that each individual's brain (or at least the tissue involved in processing static visual images) can be considered an instantiation of a 'common' brain, with activity patterns varying along similar dimensions in a common shared representational space. Aspects of this hypothesis are already strongly supported: most human brains have localized tissue responsive to specific types of stimuli, like faces and scenes. Additionally, several continuous dimensions of high-level visual selectivity have been identified across the ventral temporal cortex (Huth et al., 2012), including dimensions like animate/inanimate, large/small (based on real-world size) (Long et al., 2018), and spiky/round (Bao et al., 2020). Retinotopic organization is another example of a shared representational space, as each individual brain instantiates a unique anatomical mapping from retinal coordinates to cortical representations, and adaptive models can be estimated to transform activation patterns from individual brains to this common shared retinotopic coordinate system (Sprague & Serences, 2013; Wandell & Winawer, 2015). We analyze the similarity of representation spaces from different perspectives of common concepts, visual analysis, and eigenvectors in the following subsections. Finally, we reflect on the different ways of aligning the common representations.

Existing works, such as MindEye2 (Scotti et al., 2024), employ a simple linear adapter network to project subject-specific fMRI signals into a common representation space. A key indication of the existence of such a shared space is the structural similarity of embeddings across subjects. To explore this, we first use a pre-trained MindEye2 model to extract common-space embeddings for the shared images (the test set in MindEye2) across all subjects. Initial cosine similarity between the embeddings from different subjects is low. However, after applying an orthogonal transformation using Procrustes analysis (Schönemann, 1966), the cosine similarity improves, suggesting that the embeddings can be

structurally aligned. Despite this improvement, the alignment is not perfect, likely due to the limitations of linear transformations.



(a) Weak alignment before an orthogonal transformation. (b) Improved alignment after orthogonal transformation. (c) Near perfect alignment with nonlinear adapters.

Figure 1. Cosine similarity of shared image embeddings in the common space. (a) The alignment is weak before an orthogonal transformation. (b) Alignment improves after orthogonal transformation. (c) Near perfect alignment is achieved with nonlinear adapters and explicit alignment. Only subjects 1, 2, 5, and 7 are considered in this plot, as these subjects were used during training.

As a preliminary experiment, we pre-trained a single-subject model with a non-linear adapter and explicitly mapped subsequent subjects to this reference subject using subject-specific non-linear adapters. This approach results in near-perfect alignment in the common space. Although existing methods do not explicitly align subject-specific representations, we observed significant semantic and structural similarities across subjects’ representations. Furthermore, it is possible to map one subject’s representations to another’s using non-linear adapters. While this alignment in the common space is nearly perfect, it does not directly translate to better reconstruction performance.

We also analyze the singular vectors from the adapter weights to present semantic category analysis and images in the representation space to perform visual analysis. We present our results and analysis in the Appendix Section C. This evidence supports the core hypothesis of our work: it is possible to construct an aligned, subject-agnostic common space. In Section 3, we empirically test this hypothesis by mapping a new subject to a reference subject during training and evaluating its reconstruction performance. Additional analysis is provided in Appendix B.

### 3. fMRI Reconstruction

Building a common brain representation requires constructing an efficient fMRI reconstruction pipeline. Our approach is guided by two primary objectives: 1) achieving competitive reconstruction performance and 2) prioritizing efficiency over marginal performance gains. We hypothesize that it is possible to pre-train a single reference brain and align subsequent subjects to this reference using subject-specific adapters, significantly reducing the computational

cost while maintaining high reconstruction quality.

### 3.1. Dataset

We use the Natural Scenes Dataset (NSD) (Allen et al., 2022) but apply a different split compared to the traditional setup. Typically, common images across subjects are assigned to the test set, while the training set consists of unique images viewed by each subject. However, for effective Common Space Alignment, it is critical to have a one-to-one mapping of images across subjects. To achieve this, we incorporate the common images into the training set and swap an equal amount of training images to the test sets. This means that every subject now has a unique set of images on which they are tested. The test split is chosen to roughly ensure an equal distribution across different categories in the dataset. We present the performance of the original training method and the proposed technique on the new split to ensure a fair comparison across subjects and alignment techniques.

Our initial experiments revealed that models performed slightly worse on the unique image test set than on the common image test set, suggesting that the unique image test set presents a more challenging benchmark. Similar to prior work, we focus on subjects 1, 2, 5, and 7, as they have complete 40-hour fMRI datasets available in NSD, enabling better reconstruction performance. These subjects provide robust data for training and evaluation, allowing us to validate our alignment and reconstruction methods comprehensively.

### 3.2. Adapter Alignment

Current approaches for training multi-subject pipelines with a common representation space typically follow an end-to-end strategy, where fMRI inputs are processed by the model and the loss is computed at the final layer to minimize the discrepancy between the ground-truth and predicted embeddings. In this setup, the common space emerges organically during training without explicit constraints. However, this approach has two key drawbacks: (1) it requires extended training to form a satisfactory common space and achieve convergence, and (2) the subject-specific embeddings in the common space are not strongly aligned, making it harder for the residual MLP to map multiple subject inputs to a unified output.

To address these challenges, we propose Adapter Alignment (AA) training. In AA, the pipeline is first pre-trained end-to-end on a single reference subject, chosen based on reconstruction performance and data availability. Among NSD subjects, Subject 1 consistently exhibited the best reconstruction performance, making it the ideal candidate for constructing the reference space. After pre-training, the output embeddings for the subject-specific adapter, particularly those corresponding to the shared images, are extracted.

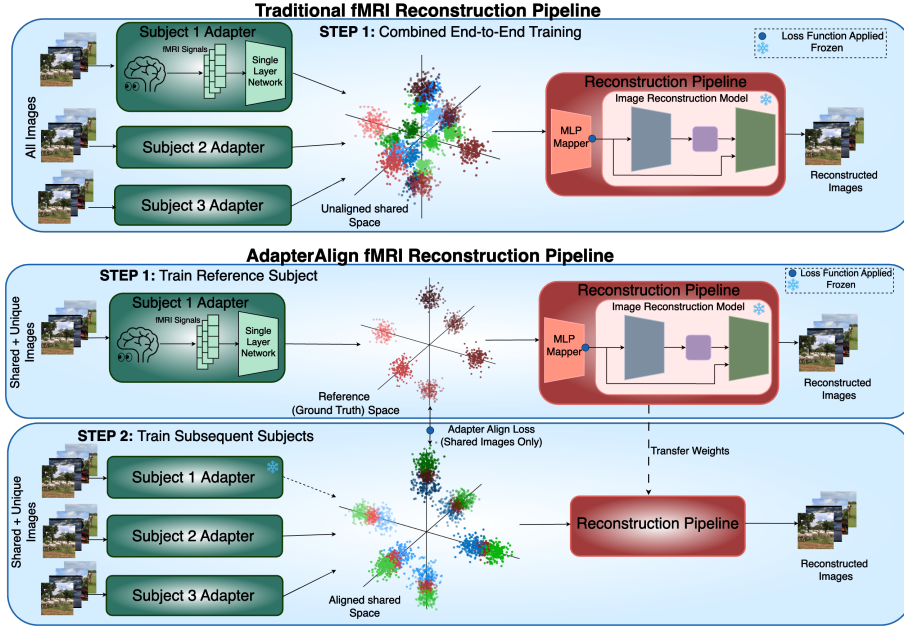


Figure 2. Training procedures for fMRI-Image Reconstruction. **Top:** Traditional Approach to reconstruction. All subjects are trained simultaneously and loss functions are applied at the MLP Mapper to align the output to pre-trained CLIP space. **Bottom:** Proposed AdapterAlign training pipeline. First you train a single reference subject and obtain their embeddings in the shared space. Then you train subsequent subjects to minimize loss at both the shared space and the mapper. The same mapper weights are transferred over in step 2.

When fine-tuning a new subject, we adopt a two-step process. First, we train the new subject’s adapter using the shared images, with the objective of aligning its output to the embeddings of Subject 1 for the same images. The adapter is allowed to overfit on these shared images until the loss is minimized. In the second step, we unfreeze the entire pipeline and resume training, applying the usual losses at the final output. Additionally, we introduce an MSE loss at the adapter level specifically for the common images, which allows the adapter to restructure itself to account for subject-specific discrepancies and adapt to the unique images encountered by the new subject. We call this process of overfitting the adapter and fine-tuning end to end “AAMax”.

This training method offers improvements in both high-data and low-data scenarios. When all training data is available, AAMax converges faster while achieving performance similar to traditional end-to-end training. However, in limited data settings, AAMax proves significantly more efficient, yielding better reconstructions and higher accuracy with fewer training samples. We outline our method in Figure 2 and break down our pipeline in the following section.

### 3.3. Reconstruction Pipeline

Our reconstruction pipeline follows a similar structure to previous works, dividing the reconstruction process into two components: a high-level semantic pipeline that maps to CLIP embeddings and a low-level visual pipeline that maps

to visual autoencoder embeddings. Both pipelines receive the same fMRI data as input but are trained separately. The outputs from both pipelines are then integrated into a pre-trained diffusion model to generate the final reconstruction. The exact training process and loss functions are presented in Appendix Sections I and J.

Flattened fMRI voxels from the nsdgeneral region are fed into a subject-specific adapter, consisting of a single linear layer with a GELU non-linearity. This maps the fMRI data into a subject-agnostic shared space. This shared-space representation is then processed by a Residual Multi-Layer Perceptron (MLP). A modality gap still exists between outputs from the MLP and the ground-truth CLIP (Radford et al., 2021) embedding space. We further incorporate a pre-trained diffusion prior based on DALL-E 2 (Ramesh et al., 2022) to bridge this modality gap. The output from the prior is the mapped CLIP embedding. This is fed as conditioning to the diffusion model.

Our high-level pipeline is based on the architecture used in MindEye1 (Scotti et al., 2023) and MindEye2 (Scotti et al., 2024), where the fMRI data is mapped to CLIP image embeddings of the corresponding source images. The pretraining phase leverages a combination of diffusion prior loss and CLIP loss. During fine-tuning, we add an additional MSE loss for the common images to further refine the

mappings. The overall loss function in this stage is:

$$\mathcal{L}_{\text{new}} = \begin{cases} \lambda_1 \mathcal{L}_{\text{Prior}} + \lambda_2 \mathcal{L}_{\text{CLIP}}, & \text{for unique images} \\ \lambda_1 \mathcal{L}_{\text{Prior}} + \lambda_2 \mathcal{L}_{\text{CLIP}} \\ + \lambda_3 \mathcal{L}_{\text{MSE}}(\mathbf{z}_{\text{new}}, \mathbf{z}_{\text{ref}}), & \text{for common images} \end{cases}$$

where  $\mathbf{z}_{\text{adapter, new}}$  and  $\mathbf{z}_{\text{adapter, ref}}$  are the adapter-level embeddings for the new and reference subjects, respectively, on the shared common images. We present a breakdown of the high level pipeline loss functions in Appendix I.

The low-level pipeline also follows a similar structure to the high-level one but maps the fMRI data to latent embeddings derived from a custom autoencoder. This autoencoder is trained on downscaled images from the NSD dataset (64x64x3) and reduces them to a latent space of size 1024. The low-level pipeline learns to map to this latent space, and passing these embeddings through a pre-trained decoder produces blurry reconstructions. The loss function for this stage is:

$$\mathcal{L}_{\text{new}} = \begin{cases} \mathcal{L}_{\text{MSE}}(\mathbf{z}_{\text{fMRI, new}}, \mathbf{z}_{\text{AE}}), & \text{for unique images} \\ \mathcal{L}_{\text{MSE}}(\mathbf{z}_{\text{fMRI, new}}, \mathbf{z}_{\text{AE}}) \\ + \mathcal{L}_{\text{MSE}}(\mathbf{z}_{\text{adapt, new}}, \mathbf{z}_{\text{adapt, ref}}), & \text{for common images} \end{cases}$$

where  $\mathbf{z}_{\text{fMRI, new}}$  is the output embedding for the new subject,  $\mathbf{z}_{\text{AE}}$  is the AE latent space representation of the image and  $\mathbf{z}_{\text{adapter, new}}$  and  $\mathbf{z}_{\text{adapter, ref}}$  are the adapter-level embeddings for the new and reference subjects, respectively. We present a breakdown of the low level pipeline loss functions in Appendix J

For the final step, the mapped CLIP embedding is used as a conditioning input to the pre-trained diffusion prior model. The low-level blurry reconstructions serve as an initialization for the diffusion model, and the final, refined reconstructions are then produced. For more architectural details, we refer readers to the MindEye1 (Scotti et al., 2023) and MindEye2 (Scotti et al., 2024) papers.

### 3.4. Tests on Complete Data

We first validate our training method using the full dataset. Subject 1 is used as the reference subject, while fine-tuning is performed on Subjects 2, 5, and 7. The results are presented in Table 1. We use the same set of metrics as Scotti et al. (2024) to evaluate our reconstructions. Pixel Correlation, SSIM and 2-way percent correct for the 2nd and 5th layer of AlexNet are considered low level visual metrics. 2-way percent correct for Inception(Szegedy et al., 2016), CLIP, EfficientNet(Tan, 2019) and SwAV(Caron et al., 2020) score are considered high level metrics. When trained to completion, both methods—end-to-end training and adapter alignment—show similar overall performance. However, the MSE loss at the adapter level is significantly lower (by

an order of magnitude as shown in Appendix B.2) when using adapter alignment. This allows for more precise post-hoc analysis after extracting embeddings from the common space.

Additionally, we observe that adapter alignment yields better results than regular end-to-end training when the model is trained for fewer epochs, with faster convergence. Both approaches eventually reach similar performance levels, as shown in Figure 3.

Table 1. Quantitative results on training the reconstruction models on all 40 hours of data. Both methods perform similarly across all metrics.

Method	Low-Level				High-Level			
	PixCorr ↑	SSIM ↑	Alex(2) ↑	Alex(5) ↑	Incep ↑	CLIP ↑	Eff ↓	SwAV ↓
Subj1 Pretraining	0.345	0.346	92.80%	96.88%	94.40%	90.02%	0.692	0.399
Normal FineTune Avg	0.258	<b>0.339</b>	<b>89.64%</b>	95.05%	92.63%	<b>89.64%</b>	0.717	0.427
AAMax FineTune Avg	<b>0.259</b>	0.337	89.20%	<b>95.09%</b>	<b>92.68%</b>	89.49%	<b>0.713</b>	<b>0.423</b>
Subj2 FineTune Normal	0.294	<b>0.345</b>	91.42%	95.92%	<b>93.00%</b>	88.68%	0.721	0.425
Subj2 FineTune AAMax	<b>0.295</b>	0.340	<b>91.52%</b>	<b>96.20%</b>	92.96%	<b>89.87%</b>	<b>0.707</b>	<b>0.409</b>
Subj5 FineTune Normal	0.236	<b>0.335</b>	<b>89.45%</b>	<b>95.32%</b>	93.98%	<b>91.63%</b>	0.701	0.419
Subj5 FineTune AAMax	<b>0.240</b>	0.332	88.60%	95.16%	<b>94.04%</b>	90.71%	<b>0.698</b>	<b>0.413</b>
Subj7 FineTune Normal	<b>0.244</b>	0.339	<b>88.06%</b>	<b>93.91%</b>	90.92%	<b>88.61%</b>	<b>0.731</b>	<b>0.438</b>
Subj7 FineTune AAMax	0.242	<b>0.340</b>	87.48%	<b>93.91%</b>	<b>91.05%</b>	87.89%	0.734	0.448

### 3.5. Tests on Limited Data

A key objective of multi-subject pipelines is to achieve satisfactory models of new subjects with limited data. Acquiring fMRI data is costly, and reducing the data requirements for modeling a subject’s brain makes fMRI reconstruction more accessible. MindEye2 demonstrated that fine-tuning a new subject with as little as 1 hour of data is possible, though the resulting reconstructions leave room for improvement.

In our experiments, we evaluate the fine-tuning of a new subject in three scenarios: 1 hour, 2 hours, and 4 hours of training data. The NSD dataset provides 40 hours of data per subject, all of which is used for the full data tests in Section 3.4. For this experiment, we designate Subject 5 as the reference subject and fine-tune Subject 1 using the shared images. We compare the performance of normal end-to-end training and Adapter Alignment (AA), with results presented in Table 11.

Adapter Alignment consistently outperforms the end-to-end approach, showing significant improvements even after just one epoch of training. The performance gap widens as the amount of fine-tuning data is reduced. Due to the lightweight nature of Adapter Alignment, which involves training on just 250 images using a single layer, the time required to align the adapter is minimal compared to full end-to-end training. We present the training times for both methods in Appendix Section G. In fact, even after 160 epochs of normal training, the model’s performance fails to match the Epoch 1 results of Adapter Alignment. Figure 4 illustrates the reconstruction performance across epochs for

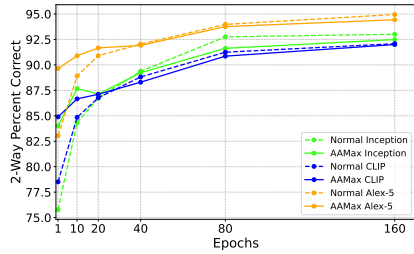


Figure 3. Comparing finetuning reconstruction performance over time with all the data. From left to right: (a) High level metrics over time for Subject 1. Both methods perform similarly but the normal method takes about 20 epochs to match AAMax’s numbers (b) Example reconstruction over time. The top row is the normal pipeline and the bottom row is the Adapter alignment pipeline.

both methods.

Table 2. Quantitative results on fine tuning a new subject with limited data. FT=Fine tuning. The first section shows the result of fine tuning with 250 images after 1 epoch and after 160 epochs using normal end-to-end training vs AAMax. The second section compares performance on 500 images and the third section compares performance on 1000 images. In all cases AAMax, significantly outperforms normal training. The greyed out low level metrics are not optimized for in these experiments.

Method	Low-Level				High-Level			
	PixCorr ↑	SSIM ↑	Alex(2) ↑	Alex(5) ↑	Incep ↑	CLIP ↑	Eff ↓	SwAV ↓
Subj1 FT NS 250 Normal E1	0.031	0.234	58.31%	62.56%	58.51%	58.71%	0.947	0.611
Subj1 FT NS 250 AAMAX E1	0.095	0.254	77.20%	85.98%	78.80%	79.39%	0.833	0.503
Subj1 FT NS 250 Normal E160	0.094	0.239	71.54%	80.10%	73.11%	74.02%	0.875	0.537
Subj1 FT NS 250 AAMAX E160	0.105	0.259	76.77%	86.20%	<b>80.08%</b>	<b>80.14%</b>	<b>0.828</b>	<b>0.496</b>
Subj1 FT NS 500 Normal E1	0.049	0.242	62.41%	68.06%	62.64%	64.80%	0.925	0.583
Subj1 FT NS 500 AAMAX E1	0.112	0.275	79.46%	88.29%	<b>83.28%</b>	82.61%	0.803	0.485
Subj1 FT NS 500 Normal E160	0.110	0.270	75.32%	84.62%	76.66%	78.55%	0.845	0.516
Subj1 FT NS 500 AAMAX E160	0.114	0.285	80.00%	88.50%	83.19%	<b>83.05%</b>	<b>0.799</b>	<b>0.480</b>
Subj1 FT NS 1000 Normal E1	0.079	0.241	65.84%	73.04%	64.19%	68.10%	0.914	0.574
Subj1 FT NS 1000 AAMAX E1	0.129	0.265	80.83%	90.93%	<b>86.66%</b>	86.17%	0.767	0.460
Subj1 FT NS 1000 Normal E160	0.124	0.253	77.86%	89.18%	83.10%	83.26%	0.801	0.480
Subj1 FT NS 1000 AAMAX E160	0.127	0.273	81.73%	91.29%	86.23%	<b>86.26%</b>	<b>0.763</b>	<b>0.453</b>

## 4. Best Candidate Image Selection

Here, we present a selection algorithm that significantly reduces the amount of data required to train a model for a new subject. Later, we carry out an empirical analysis of the method.

### 4.1. Greedy Algorithm

In the context of fMRI-based visual reconstruction, we introduce a greedy algorithm that selects the most representative subset of images from the common space. We begin with an embedding of the common set of images into a representation space and choose the first  $d$  dimensions corresponding to the principal singular vectors. For each dimension  $j$ , we partition the range into  $B_j$  bins that is determined by the ratio of singular value  $\lambda_j$  to the largest singular value  $\lambda_1$ :

$$B_j = \left\lceil w \cdot \frac{\lambda_j}{\lambda_1} \right\rceil, \quad j = 1, 2, \dots, d$$

where  $w$  is a predefined scaling parameter. Dimensions with larger singular values are partitioned into more bins, reflecting their greater variance and importance in capturing meaningful data features.

Each image (and its fMRI) maps to exactly one bin in each dimension. Our goal is to find the smallest subset of images that covers all bins in each dimension. This subset is critical in selecting the most representative images for a new subject, ensuring that the selected images capture the key activity patterns that generalize across subjects. The problem as stated is NP-hard. However, it is submodular and a greedy heuristic such as given below achieves an  $(1 - 1/e)$  approximation ratio.

Given a subset  $S$  of images, let  $Gap(S, j)$  be the number of empty bins in dimension  $j$ , and let  $Gap(S) = \sum_j Gap(S, j)$  be the total number of images across all dimensions. At every step, the greedy algorithm chooses image  $i \notin S$  that minimizes  $Gap$  when added to  $S$ .

After acquiring the selected images, we train a ridge regression layer on this subset, which then serves as an adapter for the remainder of the pipeline. With only a minimal number of additional end-to-end training epochs, our approach achieves comparable performance while relying on a substantially smaller training set. Section F in the Appendix provides additional details about the algorithm, while Section E contains the proof of the submodularity property.

### 4.2. Results

We achieve better results on high-level metrics compared to the baseline while reducing the required data by 50%. Figure 5 (a) illustrates how Inception and CLIP distances fluctuate as a function of the amount of training data for subject 2. Figure 5 (b) presents the model’s performance when 150 images are selected for the training set, while varying the number of principal eigenvectors onto which the embeddings are projected. Differences in the performance for different numbers of dimensions are likely due to the nature of the binning process, as the number of bins created along

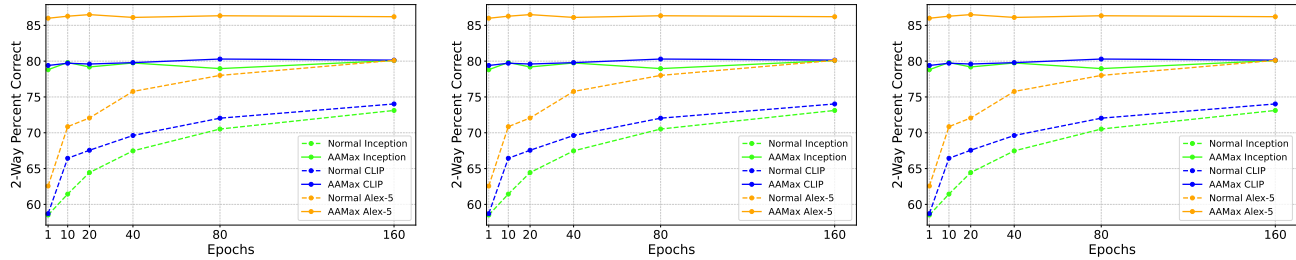


Figure 4. Comparing finetuning reconstruction performance over time with limited data. From left to right: (a) Finetuning Subject 1 with 250 images or 1 hour of data (b) Finetuning Subject 1 with 500 images or 2 hours of data (c) Finetuning Subject 1 with 1000 images or 3 hours of data. We observe that adapter alignment (AAMax) not only outperforms normal end-to-end training, but the performance at Epoch 1 is better than the normal method’s performance at Epoch 160.

the eigenvectors provides better coverage. Further analysis of this behavior presents an interesting direction for future work, especially considering that, as Appendix H demonstrates, the optimal number of eigenvectors varies across subjects. Our method highlights the critical role of strategic data selection in achieving superior performance. For additional details on the experimental performance, please refer to section H in the Appendix.

As shown in Table 3, this integrated approach outperforms conventional finetuning.

Table 3. Performance metrics when fine-tuning for Subject 2. *Regular FT* stands for regular fine-tuning (row 1). *AA* stands for adapter alignment (row 2). *AA + IS* stands for adapter alignment with image selection (row 3).

	Low-Level				High-Level			
	PixCorr ↑	SSIM ↑	Alex(2) ↑	Alex(5) ↑	Incep ↑	CLIP ↑	Eff ↓	SwAV ↓
Regular FT	0.112	0.306	75.16%	82.06%	71.99%	72.48%	0.872	0.548
AA	<b>0.115</b>	<b>0.307</b>	76.48%	83.28%	75.37%	73.27%	0.855	0.543
AA + IS	0.113	0.298	<b>77.28%</b>	<b>85.40%</b>	<b>79.63%</b>	<b>75.12%</b>	<b>0.844</b>	<b>0.531</b>

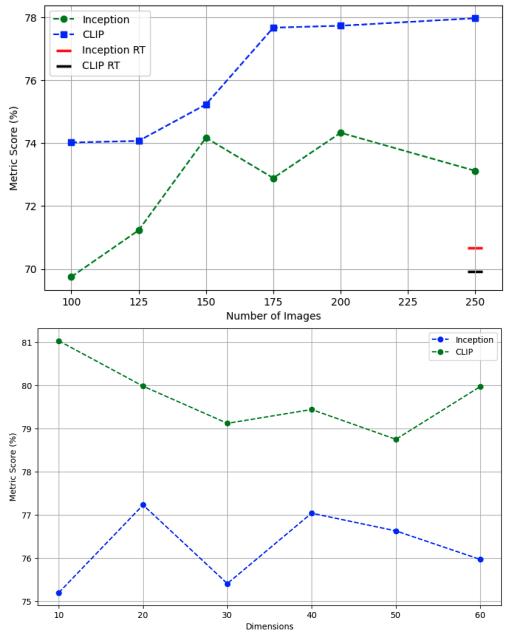


Figure 5. Comparison of the performance of the image selection strategy. Both figures display the Inception and CLIP distance metrics for subject 2. (a) Performance with varying training set sizes, where the red and black lines (labeled as Inception RF and CLIP RF) at the 250-point mark indicate the model’s performance without a data selection strategy. (b) Performance with varying numbers of principal eigenvectors.

Finally, the most significant performance gains emerge when image selection is combined with adaptive alignment.

## 5. Extending to Other Datasets

To demonstrate that our proposed method generalizes across datasets, we conducted experiments on the THINGS dataset. We used a model pre-trained on Subject 1 from the NSD dataset and fine-tuned it on Subject 1 from the THINGS dataset. Since a one-to-one mapping does not exist between the THINGS and NSD datasets, we build an implicit common set by comparing the train images of THINGS with the NSD common set to find a subset of semantically similar image pairs. CLIP is used to identify semantically similar images. In the end, 150 images are chosen as the common set for the THINGS dataset. As shown in Table 4, our AAMax method again outperforms conventional fine-tuning. This result is especially impressive as AAMax was able to semantically align the images even without an explicit alignment. We present additional experiments in Appendix Section B to show that AAMax actually improves alignment in the shared space.

Several factors may explain the observed performance differences between the two datasets. While a plurality of recent fMRI reconstruction reports have focused on analyses of the large and high-quality Natural Scenes Dataset, which measured high-SNR 7 Tesla fMRI data at a 1.8 mm resolution, such data are often out of reach for most neuroscience



Figure 6. Examples of reconstructed images from Subject 1 of the THINGS dataset after fine-tuning. Each pair depicts the ground truth (left) and the reconstructed image (right).

labs. The modal imaging setup available to many cognitive neuroscience labs is a 3T scanner, such as a Siemens Prisma, which can achieve relatively high-quality images at 2-2.5 mm resolution and reasonable sampling rate (0.5-2 s). The THINGS-fMRI dataset was recently made available, which includes high-quality 3T fMRI data acquired at 2 mm resolution (with multiband acceleration) while participants viewed images drawn from the THINGS object database. While, in principle, this dataset is very similar to the NSD, there are notable differences in SNR (7T vs 3T), stimulus presentation protocol (NSD: 3 s stimulus presentation/1 s ITI; THINGS: 0.5 s stimulus presentation/4 s ITI), stimulus set (NSD: MS-COCO, THINGS: curated object images), and task performed by participants (NSD: recognition memory on each image; THINGS: object or not?). Thus, differences in decoding or reconstruction performance are expected, and not themselves a demonstration that models do not reliably generalize across datasets.

Table 4. Quantitative results on finetuning THINGS-fMRI Subject 1 using NSD Subject 1 as the reference subject. Only the high level pipeline is trained therefore pixelwise metrics are excluded. AAMax outperforms normal finetuning even when an explicit data mapping is not available.

Method	Low-Level		High-Level			
	Alex(2) ↑	Alex(5) ↑	Incep ↑	CLIP ↑	Eff ↓	SwAV ↓
NSD Subj1 Pretraining	92.80%	96.88%	94.40%	90.02%	0.692	0.399
THINGS Subj1 Individual	68.02%	72.6%	58.8%	64.29%	0.947	0.649
THINGS Subj1 Normal FineTune	77.46%	81.07%	71.06%	73.16%	0.911	0.619
THINGS Subj1 AAMax FineTune	<b>78.27%</b>	<b>85.55%</b>	<b>74.10%</b>	<b>81.37%</b>	<b>0.902</b>	<b>0.595</b>

## 6. Related Work

Recent works have achieved impressive results by mapping fMRI data to latent diffusion model (LDM) spaces (Tagaki & Nishimoto, 2023; Scotti et al., 2023; Lu et al., 2023; Xia et al., 2024), while simultaneously integrating multiple modalities. Despite this progress, these methods have not been thoroughly tested for their generalization performance across a larger population of subjects. In other words, constructing a model for a new subject still requires retraining the model from scratch to ensure optimal performance.

Approaches like Ferrante et al. (2024) have demonstrated cross-subject brain decoding using limited data samples by aligning multiple subjects. Although the authors, like us, leveraged visual stimuli commonly used for multiple subjects, the fidelity of their reconstructed images lags behind current advancements. Scotti et al. (2024), the foundation of our method, produced significant results in image reconstruction under limited data conditions but did not fully exploit the properties of the common representation space. In contrast, our novel approach enables faster convergence and improved performance in a limited data setting by effectively leveraging the structure of the common space.

## 7. Conclusions & Discussion

In this work, we present compelling evidence for the existence of a shared visual representation space across subjects and datasets, allowing brain activity from different individuals and experimental settings to be aligned in a common space. Building on this foundation, we introduce Adapter Alignment (AA), a novel and efficient approach for subject-specific alignment in fMRI-based visual reconstruction. Our method, which is more efficient than traditional end-to-end training pipelines, achieves faster convergence and superior performance, particularly in low-data scenarios. Additionally, we propose a greedy image selection algorithm that identifies the most representative subset of images for training new subjects. This approach reduces the amount of data required for fine-tuning by up to 50% without sacrificing performance, addressing the challenge of minimizing data requirements in fMRI-based image reconstruction. Finally, we validate the robustness of our methods by testing them on different data settings.

By leveraging the structure of the common representation space, we demonstrate the feasibility of producing high-quality visual reconstructions with a significantly reduced amount of subject-specific data. Future work could explore the integration of non-linear adapters to enhance concept extraction, potentially improving the performance and flexibility of the model. Another promising direction is to extend our methodology to different pipelines, ensuring its generalizability across various architectures, thereby making the

approach architecture-agnostic.

## References

- Achiam, J., Adler, S., Agarwal, S., Ahmad, L., Akkaya, I., Aleman, F. L., Almeida, D., Altenschmidt, J., Altman, S., Anadkat, S., et al. Gpt-4 technical report. *arXiv preprint arXiv:2303.08774*, 2023.
- Allen, E. J., St-Yves, G., Wu, Y., Breedlove, J. L., Prince, J. S., Dowdle, L. T., Nau, M., Caron, B., Pestilli, F., Charest, I., et al. A massive 7t fmri dataset to bridge cognitive neuroscience and artificial intelligence. *Nature neuroscience*, 25(1):116–126, 2022.
- Bao, P., She, L., McGill, M., and Tsao, D. Y. A map of object space in primate inferotemporal cortex. *Nature*, 583(7814):103–108, 2020.
- Beliy, R., Gaziv, G., Hoogi, A., Strappini, F., Golan, T., and Irani, M. From voxels to pixels and back: Self-supervision in natural-image reconstruction from fmri. *Advances in Neural Information Processing Systems*, 32, 2019.
- Caron, M., Misra, I., Mairal, J., Goyal, P., Bojanowski, P., and Joulin, A. Unsupervised learning of visual features by contrasting cluster assignments. *Advances in neural information processing systems*, 33:9912–9924, 2020.
- Christophel, T. B., Hebart, M. N., and Haynes, J.-D. Decoding the contents of visual short-term memory from human visual and parietal cortex. *Journal of Neuroscience*, 32(38):12983–12989, 2012.
- Ester, E. F., Anderson, D. E., Serences, J. T., and Awh, E. A neural measure of precision in visual working memory. *Journal of cognitive neuroscience*, 25(5):754–761, 2013.
- Ferrante, M., Boccato, T., Ozcelik, F., VanRullen, R., and Toschi, N. Through their eyes: multi-subject brain decoding with simple alignment techniques. *Imaging Neuroscience*, 2:1–21, 2024.
- Fisher, M. L., Nemhauser, G. L., and Wolsey, L. A. *An analysis of approximations for maximizing submodular set functions—II*. Springer, 1978.
- Gaziv, G., Beliy, R., Granot, N., Hoogi, A., Strappini, F., Golan, T., and Irani, M. Self-supervised natural image reconstruction and large-scale semantic classification from brain activity. *NeuroImage*, 254:119121, 2022.
- Harrison, S. A. and Tong, F. Decoding reveals the contents of visual working memory in early visual areas. *Nature*, 458(7238):632–635, 2009.
- Hebart, M. N., Contier, O., Teichmann, L., Rockter, A. H., Zheng, C. Y., Kidder, A., Coriveau, A., Vaziri-Pashkam, M., and Baker, C. I. Things-data, a multimodal collection of large-scale datasets for investigating object representations in human brain and behavior. *Elife*, 12:e82580, 2023.
- Hendrycks, D. and Gimpel, K. Gaussian error linear units (gelus), 2023. URL <https://arxiv.org/abs/1606.08415>.
- Huth, A. G., Nishimoto, S., Vu, A. T., and Gallant, J. L. A continuous semantic space describes the representation of thousands of object and action categories across the human brain. *Neuron*, 76(6):1210–1224, 2012.
- Itthipuripat, S., Sprague, T. C., and Serences, J. T. Functional mri and eeg index complementary attentional modulations. *Journal of Neuroscience*, 39(31):6162–6179, 2019.
- Kamitani, Y. and Tong, F. Decoding the visual and subjective contents of the human brain. *Nature neuroscience*, 8(5):679–685, 2005.
- Li, H.-H., Sprague, T. C., Yoo, A. H., Ma, W. J., and Curtis, C. E. Joint representation of working memory and uncertainty in human cortex. *Neuron*, 109(22):3699–3712, 2021.
- Lin, S., Sprague, T., and Singh, A. K. Mind reader: Reconstructing complex images from brain activities. *Advances in Neural Information Processing Systems*, 35:29624–29636, 2022.
- Liu, Y., Ma, Y., Zhu, G., Jing, H., and Zheng, N. See through their minds: Learning transferable neural representation from cross-subject fmri, 2024. URL <https://arxiv.org/abs/2403.06361>.
- Long, B., Yu, C.-P., and Konkle, T. Mid-level visual features underlie the high-level categorical organization of the ventral stream. *Proceedings of the National Academy of Sciences*, 115(38):E9015–E9024, 2018.
- Lu, Y., Du, C., Zhou, Q., Wang, D., and He, H. Mind-diffuser: Controlled image reconstruction from human brain activity with semantic and structural diffusion. In *Proceedings of the 31st ACM International Conference on Multimedia*, pp. 5899–5908, 2023.
- Mozafari, M., Reddy, L., and VanRullen, R. Reconstructing natural scenes from fmri patterns using bigbigan. In *2020 International joint conference on neural networks (IJCNN)*, pp. 1–8. IEEE, 2020.
- Naselaris, T., Kay, K. N., Nishimoto, S., and Gallant, J. L. Encoding and decoding in fmri. *Neuroimage*, 56(2):400–410, 2011.

- Radford, A., Kim, J. W., Hallacy, C., Ramesh, A., Goh, G., Agarwal, S., Sastry, G., Askell, A., Mishkin, P., Clark, J., et al. Learning transferable visual models from natural language supervision. In *International conference on machine learning*, pp. 8748–8763. PMLR, 2021.
- Ramesh, A., Dhariwal, P., Nichol, A., Chu, C., and Chen, M. Hierarchical text-conditional image generation with clip latents. *arXiv preprint arXiv:2204.06125*, 1(2):3, 2022.
- Ren, Z., Li, J., Xue, X., Li, X., Yang, F., Jiao, Z., and Gao, X. Reconstructing seen image from brain activity by visually-guided cognitive representation and adversarial learning. *NeuroImage*, 228:117602, 2021.
- Schönemann, P. H. A generalized solution of the orthogonal procrustes problem. *Psychometrika*, 31(1):1–10, 1966.
- Schrijver, A. et al. *Combinatorial optimization: polyhedra and efficiency*, volume 24. Springer, 2003.
- Scolari, M., Byers, A., and Serences, J. T. Optimal deployment of attentional gain during fine discriminations. *Journal of Neuroscience*, 32(22):7723–7733, 2012.
- Scotti, P., Banerjee, A., Goode, J., Shabalin, S., Nguyen, A., Dempster, A., Verlinde, N., Yundler, E., Weisberg, D., Norman, K., et al. Reconstructing the mind’s eye: fmri-to-image with contrastive learning and diffusion priors. *Advances in Neural Information Processing Systems*, 37, 2023.
- Scotti, P. S., Tripathy, M., Villanueva, C. K. T., Kneeland, R., Chen, T., Narang, A., Santhirasegaran, C., Xu, J., Naselaris, T., Norman, K. A., et al. Mindeye2: Shared-subject models enable fmri-to-image with 1 hour of data. *arXiv preprint arXiv:2403.11207*, 2024.
- Seeliger, K., Güçlü, U., Ambrogioni, L., Güçlütürk, Y., and Van Gerven, M. A. Generative adversarial networks for reconstructing natural images from brain activity. *NeuroImage*, 181:775–785, 2018.
- Serences, J. T. and Boynton, G. M. Feature-based attentional modulations in the absence of direct visual stimulation. *Neuron*, 55(2):301–312, 2007.
- Serences, J. T., Ester, E. F., Vogel, E. K., and Awh, E. Stimulus-specific delay activity in human primary visual cortex. *Psychological science*, 20(2):207–214, 2009.
- Shen, G., Dwivedi, K., Majima, K., Horikawa, T., and Kamitani, Y. End-to-end deep image reconstruction from human brain activity. *Frontiers in computational neuroscience*, 13:432276, 2019.
- Sprague, T. C. and Serences, J. T. Attention modulates spatial priority maps in the human occipital, parietal and frontal cortices. *Nature neuroscience*, 16(12):1879–1887, 2013.
- Sprague, T. C., Ester, E. F., and Serences, J. T. Reconstructions of information in visual spatial working memory degrade with memory load. *Current Biology*, 24(18):2174–2180, 2014.
- Sprague, T. C., Itthipuripat, S., Vo, V. A., and Serences, J. T. Dissociable signatures of visual salience and behavioral relevance across attentional priority maps in human cortex. *Journal of neurophysiology*, 119(6):2153–2165, 2018.
- Szegedy, C., Vanhoucke, V., Ioffe, S., Shlens, J., and Wojna, Z. Rethinking the inception architecture for computer vision. In *Proceedings of the IEEE conference on computer vision and pattern recognition*, pp. 2818–2826, 2016.
- Takagi, Y. and Nishimoto, S. High-resolution image reconstruction with latent diffusion models from human brain activity. In *Proceedings of the IEEE/CVF Conference on Computer Vision and Pattern Recognition*, pp. 14453–14463, 2023.
- Tan, M. Efficientnet: Rethinking model scaling for convolutional neural networks. *arXiv preprint arXiv:1905.11946*, 2019.
- Wandell, B. A. and Winawer, J. Computational neuroimaging and population receptive fields. *Trends in cognitive sciences*, 19(6):349–357, 2015.
- Xia, W., de Charette, R., Oztireli, C., and Xue, J.-H. Dream: Visual decoding from reversing human visual system. In *Proceedings of the IEEE/CVF Winter Conference on Applications of Computer Vision*, pp. 8226–8235, 2024.

## A. Scaling Analysis and Projection to Higher-Dimensional Shared Spaces

We are unable to evaluate adapter alignment on the architectural set up employed by MindEye2 due to the difference in computational resources. While MindEye2 utilizes a 4096-dimensional shared space with BigCLIP and Stable Diffusion XL (SDXL), we operate under compute constraints that limit us to Versatile Diffusion. To address this limitation, we conduct a systematic scaling law analysis to evaluate how shared space dimensionality affects performance and whether adapter alignment (AAMax) continues to be effective at larger scales.

### A.1. Empirical Observations

- 1. Architectural Improvements at 1024 Dimensions:** Using a 1024-dimensional shared space, we find that BigCLIP + SDXL outperforms Versatile Diffusion, confirming that a higher-capacity CLIP space and diffusion model contribute to improved reconstruction performance.
- 2. Scaling Behavior with Versatile Diffusion:** We vary the shared space dimensionality from 512  $\rightarrow$  1024  $\rightarrow$  4096, using adapter alignment (AAMax) fine-tuning and observe consistent improvements in reconstruction quality as dimensionality increases.

This scaling behavior suggests that our approach remains agnostic to the choice of CLIP space or diffusion model, and the benefits of adapter alignment persist across dimensions.

### A.2. Projection to 4096 Dimensions with Stable Diffusion XL

The primary claim we make is that **adapter alignment is a training paradigm first and foremost**, rather than a specific architectural implementation. Our results demonstrate that adapter alignment is agnostic to both the architectural components (CLIP space, diffusion model) and the scale at which fMRI-to-image reconstruction pipelines are trained. Consequently, it should not be directly compared with works that present large-scale models, which rely on significantly higher compute budgets to achieve their performance benchmarks. Instead, adapter alignment provides a computationally efficient alternative training framework that scales effectively, making fMRI-based reconstruction more accessible even under constrained computational resources.

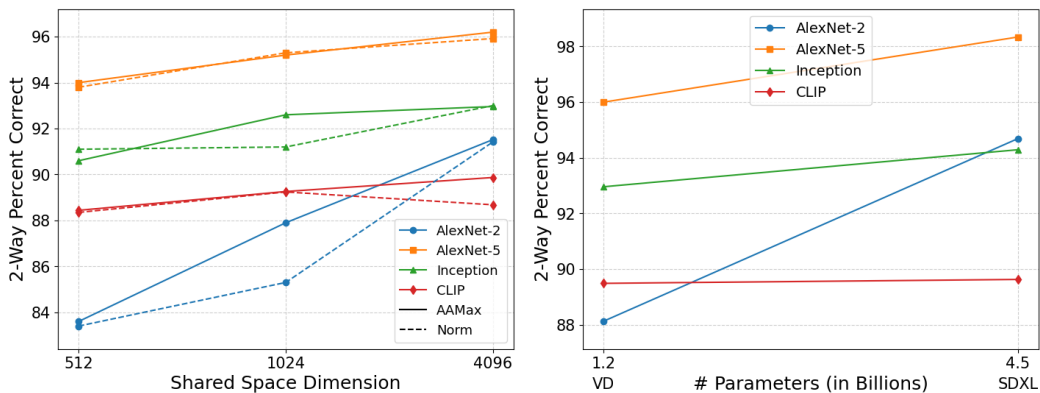


Figure 7. Comparing performance with scale for AAMax. **Left:** AAMax vs regular finetuning performance over increasing shared space size. AAMax scales with shared space dimensionality. **Right:** AAMax finetuning performance at 1024 shared space with Versatile Diffusion and Stable Diffusion XL. All metrics improve when moving to a larger diffusion model.

### A.3. Experiments with different architectures

We also present results (Table 5) where we compare normal training vs AAMax training on the MindEye2 architecture. We can observe that performance does not decline at all as we move to different architectures, as AAMax is agnostic of the size, dimensionality and the components of fMRI reconstruction pipelines.

Table 5. Performance metrics when fine-tuning for Subject 2 with MindEye2’s architecture. Regular FT stands for regular fine-tuning (row 2). AA stands for adapter alignment (row 3). These results are computed when training on the entire dataset for 200 epochs.

	Low-Level				High-Level			
	PixCorr $\uparrow$	SSIM $\uparrow$	Alex(2) $\uparrow$	Alex(5) $\uparrow$	Incep $\uparrow$	CLIP $\uparrow$	Eff $\downarrow$	SwAV $\downarrow$
Subj1 Pretraining	0.291	0.398	95.81%	98.55%	94.21%	90.15%	0.679	0.388
Subj2 Normal FT	0.108	0.347	93.25%	97.61%	90.57%	87.04%	0.844	0.543
Subj2 AAMax FT	<b>0.218</b>	<b>0.352</b>	<b>95.37%</b>	<b>97.78%</b>	<b>91.97%</b>	<b>88.76%</b>	<b>0.711</b>	<b>0.531</b>

## B. Common Space Empirical Analysis

We run several empirical tests to validate the effectiveness of Adapter Alignment in aligning the common space across subjects. For any test that requires a one-to-one mapping we use the common images else we use the test set to perform our analysis.

### B.1. Eigenvector Analysis

To first investigate the structural alignment of embeddings across subjects, we analyzed the subject-wise cosine similarity of the principal eigenvectors in the embedding spaces produced by two techniques: the standard end-to-end training (Normal) and our proposed approach (AAMax). For both techniques, we extracted the top five principal eigenvectors from the test data for each subject and computed the cosine similarity between the eigenvectors from different subjects. In normal end-to-end

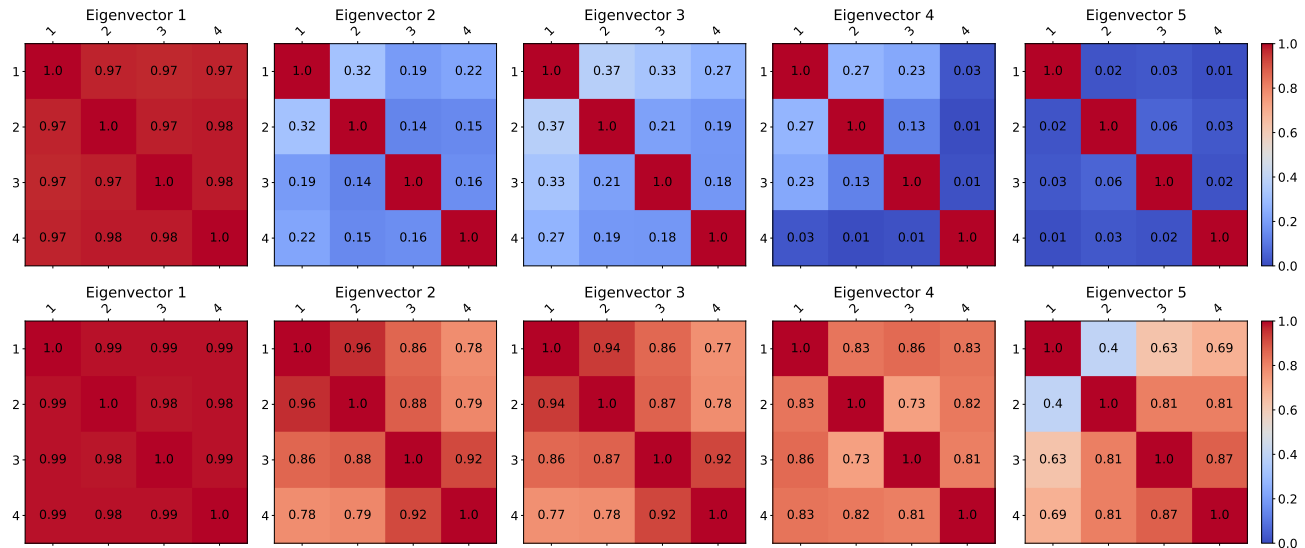


Figure 8. Comparing eigenvector cosine similarity for the test data across subjects in both training techniques. We use the first 5 principal eigenvectors. Row 1 shows the results for normal end-to-end training. Except for the first eigenvector, cosine similarity is very low across subjects. Row 2 shows the results for AAMax training. Cosine similarity is high even at the 5th principal eigenvector.

training, we observed consistently low cosine similarity between all but the first principal eigenvector of different subjects, suggesting that the primary directions of variance captured by the embeddings were highly subject-specific and lacked alignment across subjects. This indicates that the embedding space learned in this approach does not generalize well to a common structure, resulting in subject-specific representations that diverge significantly in terms of principal variance.

In contrast, AAMax training showed significantly higher cosine similarity between the principal eigenvectors of different subjects. This indicates that AAMax effectively aligns the embeddings across subjects in terms of the primary directions

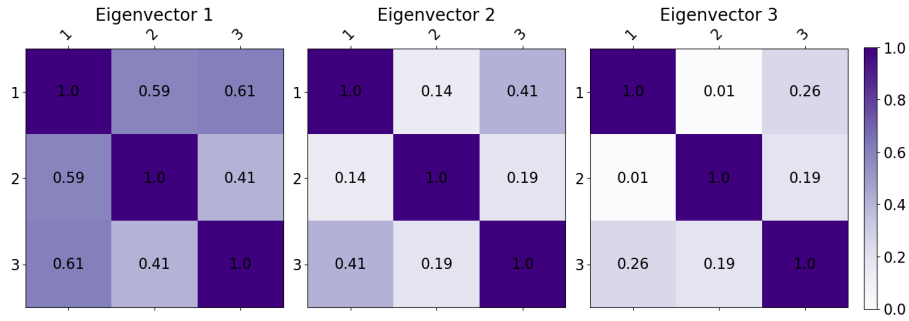


Figure 9. Comparing eigenvector cosine similarity for the test data across datasets in both training techniques. 1. Reference Subject 1 NSD 2. Normal Finetune Subject 1 THINGS 3. AAMax Finetune Subject 1 THINGS. AAMax training generates better aligned embedding spaces.

of variance, achieving a shared representation space that better captures common structural features. The high similarity across subjects reflects AAMax’s ability to encode the principal semantic and structural patterns consistently, making it more robust and generalizable compared to the normal end-to-end method.

We also perform a similar analysis across datasets in Figure 9. We compare the alignment between Subject 1 from NSD and Subject 1 from THINGS when the latter has been finetuned on a model that was pre-trained with the former. We present the difference between both training techniques. AAMax training generates better aligned embedding spaces.

### B.2. Mean Squared Error

We compare the end-to-end training approach with AAMax by evaluating the MSE between subjects using shared images after training. In the end-to-end model, we observe relatively high MSE between subjects, indicating poor alignment in the common space. In contrast, the MSE for AAMax is an order of magnitude lower, demonstrating a much stronger alignment of subject-specific embeddings. This result suggests that AAMax significantly enhances alignment across subjects, making it far more effective than the normal approach in bringing embeddings closer together in the common space.

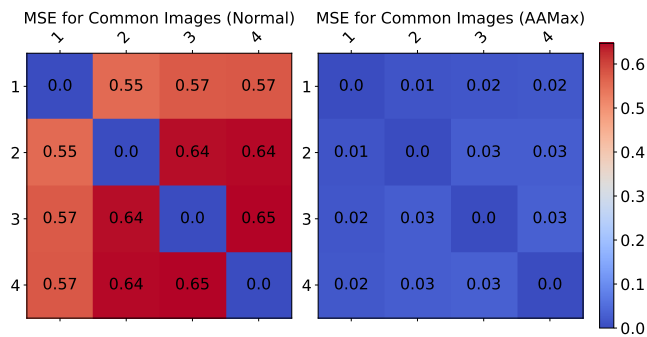


Figure 10. Comparing Mean Squared Error for the shared images across subjects in both training techniques. The MSE is compared after training is completed in both techniques. MSE for AAMax is an order of magnitude lower than normal end-to-end training

### B.3. k-Nearest Neighbor Consistency

We also evaluate the k-nearest neighbors (k-NN) consistency between subjects for shared images after training, using 50 nearest neighbors as the metric. In the end-to-end model, the k-NN consistency is relatively low, indicating that the nearest neighbors of embeddings from one subject do not align well with those from another subject. However, with AAMax, the k-NN consistency significantly improves, demonstrating much better alignment of subject-specific embeddings. AAMax consistently outperforms the normal approach, highlighting its effectiveness in preserving semantic relationships across subjects in the common space.

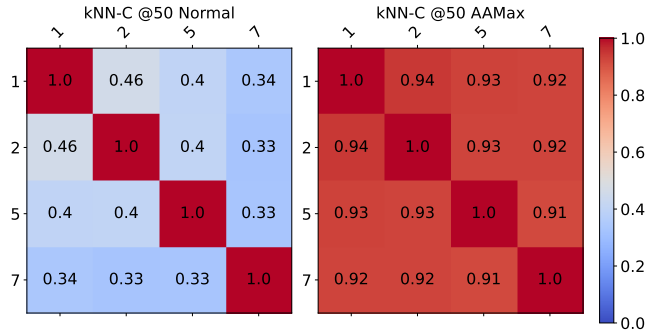


Figure 11. Comparing kNN consistency @ 50 for the shared images across subjects in both training techniques. The kNN-C is compared after training is completed in both techniques. AAMax significantly outperforms end-to-end training.

### C. Emergence of Common Concepts: Additional Details

The existence of a semantic common representation space is suggested from the emergence of semantic categories in this space. For this, we extracted the most significant left singular vectors from the ridge regression weight matrix. This matrix was extracted from the pre-trained MindEye2 (Scotti et al., 2024) model which was trained using the 1024-dimensional common space. Subsequently, we projected the 1024-dimensional embeddings of each image onto these vectors and sampled from the two extremes (set 1 and set 3) and the middle (set 2). In order to obtain an objective classification, we presented these sets of images to GPT-4o (Achiam et al., 2023) and asked it to find the semantic categories that are well represented in set 1, somewhat represented in set 2 and not represented in set 3. Results for the first five singular vectors are shown in Table 6. As is evident, images in the principal dimensions of the representation space have a common theme.

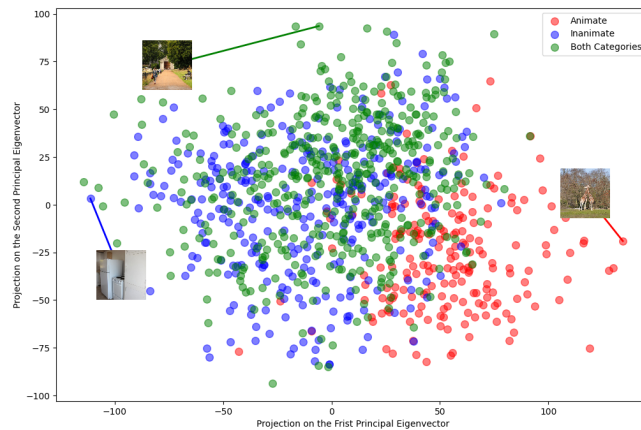


Figure 12. Visualization of the Animate/Inanimate semantic category on the two principal singular vectors. Each point (embedding) is colored based on whether its corresponding image contains ‘objects’ that fall into the Animate category (red), Inanimate category (blue) or both categories (green).

Previous studies, such as those by (Huth et al., 2012), have indicated that animal categories, including humans, are represented distinctly from non-animal categories within the brain. In our study, we observed that the common representational space also preserves these semantic properties. As demonstrated in Figure 12, after projecting the fMRI signals of Subject 2 into the common space and onto the first two singular vectors, we can see the animal vs. non-animal distinction, consistent with previous hypotheses. Extending this analysis across additional dimensions, we observed similar separations between other hypothesized semantic categories of “Social interaction,” “man-made vs nature,” and “biological vs non-biological.”

To determine if dominant semantic categories were present within these sets, we employed ChatGPT with the query: “Is there a dominant semantic category to which the majority of images in a set belong?” The methodology for defining semantic categories was consistent with that used in (Huth et al., 2012). Table 6 illustrates our findings.

Table 6. Concept analysis of images along principal dimensions.

DIMENSION 1	ANIMALS (GIRAFFES, ZEBRAS, AND ELEPHANTS), NATURE, AND OUTDOOR SCENES
DIMENSION 2	CATS AND FOOD
DIMENSION 3	KITE FLYING, AIRPLANES, AND FLYING OBJECTS
DIMENSION 4	SURFING, WATER SPORTS, BEACH, AND OCEAN SCENES
DIMENSION 5	AIRPLANES, FLYING OBJECTS, OUTDOOR ACTIVITIES AND EVENTS, TRANSPORTATION SCENES

After projecting the fMRI signals of individual images from Subject 2 into the common space and onto the first singular vectors, we observe that certain concepts are strongly represented along these dimensions defined by the singular vectors, aligning with previous hypotheses (Figures 13, 14).

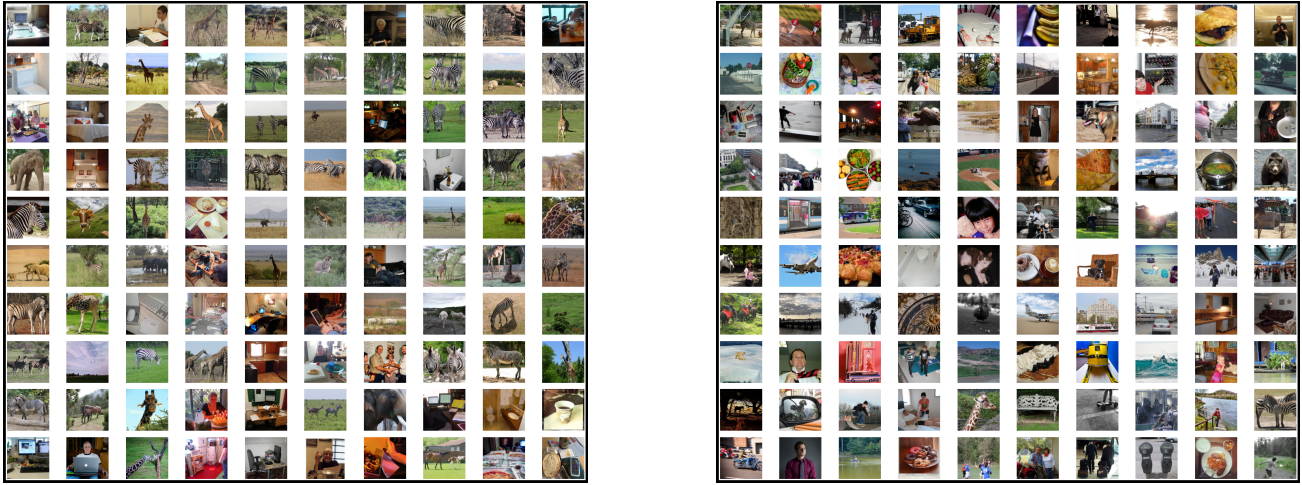


Figure 13. Comparison of images from Subject 2 with the highest and lowest projection values along the first principal left eigenvector. (a) Images whose corresponding 1024-dimensional embeddings yielded the highest projection values. (b) Images whose corresponding 1024-dimensional embeddings yielded the lowest projection values. The presence of the animate concept (e.g., giraffes, zebras, elephants) is prominent in the first set, while it fades in the second.

## D. NP-Hardness Proof

We provide a formal proof that the bin-mapping problem is NP-hard by reduction from the Set Cover problem. The proof generalizes to an arbitrary number of bins per dimension and demonstrates the equivalence between a solution to the bin-mapping problem and a solution to the Set Cover problem.

### D.1. Problem Definition

The bin-mapping problem is defined as follows:

**Definition D.1** (Bin-Mapping Problem). Given a set of  $n$ -dimensional vectors, each mapping to one of  $m$  bins per dimension, and a target  $k$ , the decision problem asks whether there exists a subset of  $k$  vectors that spans all  $m$  bins in every dimension.

### D.2. Reduction from Set Cover

We reduce the well-known Set Cover problem, which is NP-hard, to the bin-mapping problem.

**Definition D.2** (Set Cover Problem). Let  $\mathcal{U}$  be a finite universe, and let  $\mathcal{S} = \{S_1, S_2, \dots, S_l\}$  be a collection of subsets of  $\mathcal{U}$ . The Set Cover problem asks whether there exists a subcollection  $\mathcal{S}' \subseteq \mathcal{S}$  of size  $k$  such that  $\bigcup_{S \in \mathcal{S}'} S = \mathcal{U}$ .

**Theorem D.3.** *The bin-mapping problem is NP-hard.*

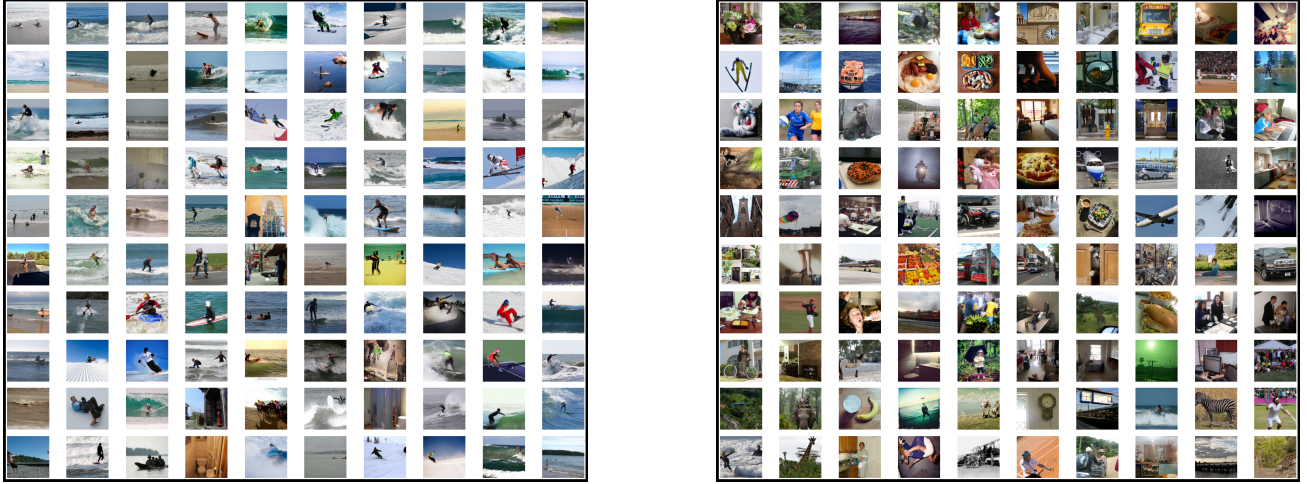


Figure 14. Comparison of images from Subject 2 with the highest and lowest projection values along the 4<sup>th</sup> principal left eigenvector. (a) Images whose corresponding 1024-dimensional embeddings yielded the highest projection values. (b) Images whose corresponding 1024-dimensional embeddings yielded the lowest projection values. Again the presence of common concepts (e.g. surfing, water sports, beach, and ocean scenes) is prominent in the first set, while it fades in the second.

*Proof.* We reduce the Set Cover problem to the bin-mapping problem as follows:

- Let  $\mathcal{U} = \{1, 2, \dots, n\}$  represent the universe of elements.
- For each subset  $S_i \in \mathcal{S}$ , construct an  $n$ -dimensional vector  $V_i$  such that:
  - For every element  $d \in S_i$ , the vector  $V_i$  places  $d$  in  $\text{Bin}_1$  in the corresponding dimension.
  - For all  $d \notin S_i$ , the vector  $V_i$  places  $d$  in  $\text{Bin}_2$ .
- Add two special vectors  $N_2$  and  $N_3$ :
  - $N_2$  covers  $\text{Bin}_2$  in all dimensions.
  - $N_3$  covers  $\text{Bin}_3$  in all dimensions.

### Key Properties of the Construction:

1. Each  $V_i$  corresponds to a subset  $S_i \in \mathcal{S}$ .
2. Any collection of input subsets  $\mathcal{S}'$  leaves a hole in  $\text{Bin}_2$  and  $\text{Bin}_3$  in at least one dimension.
3. The special vectors  $N_2$  and  $N_3$  are necessary to fill these holes.
4. A set of vectors  $\mathcal{V}' \subseteq \mathcal{V}$  forms a bin cover if and only if the corresponding subset  $\mathcal{S}'$  forms a set cover.

**Correctness:** A solution to the Set Cover problem maps directly to a solution to the Bin-Mapping problem:

- If  $\mathcal{S}'$  is a set cover, then  $\mathcal{S}' \cup \{N_2, N_3\}$  forms a bin cover.
- Conversely, if  $\mathcal{V}'$  is a bin cover, then  $\mathcal{V}' \setminus \{N_2, N_3\}$  corresponds to a set cover.

Since the Set Cover problem is NP-hard, and we have reduced it to the bin-mapping problem, the bin-mapping problem is also NP-hard. □

## E. Proof of Approximation Ratio

In this section, we prove that the gap function  $\text{Gap}(S)$ , minimized by our greedy heuristic, satisfies the submodularity property. Submodularity guarantees the diminishing returns property, which forms the basis for the  $1 - \frac{1}{e}$  approximation ratio achieved by the greedy algorithm for submodular optimization (Fisher et al., 1978).

### E.1. Gap Function Definition

The gap function measures the total number of uncovered bins across all eigenvector dimensions:

$$\text{Gap}(S) = \sum_{j=1}^d \text{Gap}(S, j),$$

where  $\text{Gap}(S, j)$  is the number of bins in dimension  $j$  not covered by the subset  $S$ . A bin in dimension  $j$  is covered if any image  $i \in S$  falls into that bin.

### E.2. Submodularity Property

A function  $f(S)$  is submodular if it satisfies the diminishing returns property (Schrijver et al., 2003):

$$f(A \cup \{x\}) - f(A) \geq f(B \cup \{x\}) - f(B), \quad \forall A \subseteq B, x \notin B.$$

For the gap function, this translates to:

$$\text{Gap}(A \cup \{x\}) - \text{Gap}(A) \geq \text{Gap}(B \cup \{x\}) - \text{Gap}(B),$$

where  $A \subseteq B$  and  $x \notin B$ .

### E.3. Proof of Submodularity

Let us consider a single dimension  $j$  and define  $\Delta_A(x, j)$  as the number of bins in  $j$  covered by  $x$  but not by  $A$ :

$$\Delta_A(x, j) = \text{Gap}(A, j) - \text{Gap}(A \cup \{x\}, j).$$

Adding an image  $x$  to a subset  $A$  can only cover bins that are not already covered. Since  $A \subseteq B$ , all bins covered by  $A$  are also covered by  $B$ . Therefore, the additional bins covered by  $x$  when added to  $A$  are at least as many as those covered when adding  $x$  to  $B$ :

$$\Delta_A(x, j) \geq \Delta_B(x, j), \quad \forall j.$$

Summing over all dimensions, the total reduction in the gap function satisfies:

$$\text{Gap}(A \cup \{x\}) - \text{Gap}(A) = \sum_{j=1}^d \Delta_A(x, j),$$

$$\text{Gap}(B \cup \{x\}) - \text{Gap}(B) = \sum_{j=1}^d \Delta_B(x, j).$$

Since  $\Delta_A(x, j) \geq \Delta_B(x, j)$  for all  $j$ , we conclude:

$$\text{Gap}(A \cup \{x\}) - \text{Gap}(A) \geq \text{Gap}(B \cup \{x\}) - \text{Gap}(B).$$

Thus,  $\text{Gap}(S)$  satisfies the submodularity property.

### E.4. Monotonicity of $\text{Gap}(S)$

The gap function  $\text{Gap}(S)$  is also monotone non-increasing because adding more elements to  $S$  can only reduce (or leave unchanged) the number of uncovered bins:

$$\text{Gap}(A \cup \{x\}) \leq \text{Gap}(A).$$

## E.5. Conclusion

Since  $\text{Gap}(S)$  is both submodular and monotone, the greedy algorithm applied to minimize the gap function achieves a  $1 - \frac{1}{e}$  approximation ratio (Fisher et al., 1978).

## F. Greedy Image Selection Algorithm

Algorithm 1 presents the greedy heuristic for bin-coverage that is utilized in the data selection method.

---

**Algorithm 1** Greedy Heuristic for Bin Coverage

---

**Require:** Set of images  $\mathcal{I}$ , parameter  $w$

**Ensure:**  $S$ : Subset of images covering all bins

- 1: Initialize  $S \leftarrow \emptyset$
  - 2: Define  $\text{Gap}(S, j)$ : Number of empty bins in dimension  $j$
  - 3: Define  $\text{Gap}(S) \leftarrow \sum_j \text{Gap}(S, j)$
  - 4: **for** each dimension  $j = 1, 2, \dots, d$  **do**
  - 5:   Compute the number of bins  $B_j = \left\lfloor w \cdot \frac{\lambda_j}{\lambda_1} \right\rfloor$
  - 6: **end for**
  - 7: **while**  $\text{Gap}(S) > 0$  **do**
  - 8:   Select  $i \in \mathcal{I} \setminus S$  minimizing  $\text{Gap}(S \cup \{i\})$
  - 9:   Update  $S \leftarrow S \cup \{i\}$
  - 10: **end while**
- 

## G. Training Time

Table 7. Comparison of Training Times for Normal and AAMax Training Methods. Numbers are averaged over all 3 fine tune subjects (2,5,7). The Adapters are first allowed to overfit by training them upto 400 epochs using MSE loss. This takes around a minute. Then end-to-end alignment is performed. It is important to note that besides the addition of the MSE Loss at the adapter level, both pipelines are running the same architecture and data and performance is thus very similar. The final time given is the time to train up to 160 epochs. But AAMax training can outperform 160 epochs of Normal training with just one epoch of end-to-end alignment.

Training Method	Adapter Alignment (Total Time)	End-to-End Fine tuning		Total Time to Train
		Time per Epoch	Total Time (160 epochs)	
Normal Training	-	221.4 seconds	590.4 minutes	590.4 minutes
AAMax Training	67 seconds	223.61 seconds	596.21 minutes	597.4 minutes

## H. Additional Experimental Results

### H.1. Best Candidate Image Selection: Additional Evaluation

We conducted several experiments to demonstrate that our image selection strategy outperforms the baseline method in a limited data setting. Below we present our experimental results.

Table 8. Comparison of performance on our data selection strategy with varying number of dimensions (singular values) for **Subject 2**. Our method has not been optimized for low-level metrics, which are shown in gray for reference. 150 images were used for all the experiments in this table.

Dimensions	Low-Level				High-Level			
	PixCorr ↑	SSIM ↑	Alex(2) ↑	Alex(5) ↑	Incep ↑	CLIP ↑	Eff ↓	SwAV ↓
10	0.099	0.254	74.27%	<b>83.55%</b>	75.20%	<b>81.03%</b>	0.835	0.520
20	0.105	0.220	73.06%	83.33%	<b>77.23%</b>	79.98%	<b>0.828</b>	<b>0.508</b>
30	<b>0.119</b>	<b>0.288</b>	<b>74.51%</b>	82.11%	75.41%	79.12%	0.836	0.516
40	0.103	0.212	72.22%	83.35%	77.04%	79.44%	0.839	0.519
50	0.107	0.217	73.73%	82.76%	76.63%	78.75%	0.845	0.524
60	0.101	0.202	72.91%	83.49%	75.97%	79.97%	0.829	0.519

Table 9. Comparison of performance on our data selection strategy with varying number of dimensions (singular values) for **Subject 5**. Our method has not been optimized for low-level metrics, which are shown in gray for reference. 150 images were used for all the experiments in this table.

Dimensions	Low-Level				High-Level			
	PixCorr ↑	SSIM ↑	Alex(2) ↑	Alex(5) ↑	Incep ↑	CLIP ↑	Eff ↓	SwAV ↓
10	<b>0.138</b>	<b>0.292</b>	75.20%	83.81%	78.62%	83.23%	0.818	0.525
20	0.101	0.241	74.62%	84.26%	<b>80.11</b>	<b>83.97%</b>	<b>0.797</b>	<b>0.487</b>
30	0.120	0.276	<b>76.56%</b>	84.59%	78.81%	83.03%	0.816	0.507
40	0.119	0.253	76.01%	<b>85.40%</b>	79.16	83.56%	0.810	0.501
50	0.106	0.254	74.85%	83.54%	77.48%	81.83%	0.825	0.506
60	0.116	0.248	75.32%	84.55%	78.44%	82.22%	0.806	0.494

Table 10. Comparison of performance on our data selection strategy with varying number of dimensions (singular values) for **Subject 7**. Our method has not been optimized for low-level metrics, which are shown in gray for reference. 150 images were used for all the experiments in this table.

Dimensions	Low-Level				High-Level			
	PixCorr ↑	SSIM ↑	Alex(2) ↑	Alex(5) ↑	Incep ↑	CLIP ↑	Eff ↓	SwAV ↓
10 (150)	0.112	<b>0.272</b>	72.60%	80.93%	74.72%	<b>79.09%</b>	0.840	<b>0.509</b>
20 (150)	0.095	0.241	69.75%	79.95%	72.92%	77.51%	0.851	0.521
30 (150)	0.102	0.258	72.06%	80.74%	74.23%	77.92%	0.843	0.526
40 (150)	<b>0.117</b>	0.267	<b>73.23%</b>	<b>80.99%</b>	74.20%	78.15%	0.840	0.520
50 (150)	0.105	0.220	69.18%	78.17%	70.75%	75.23%	<b>0.860</b>	0.533
60 (150)	0.103	0.224	69.43%	79.77%	<b>75.07%</b>	77.13%	0.839	0.528

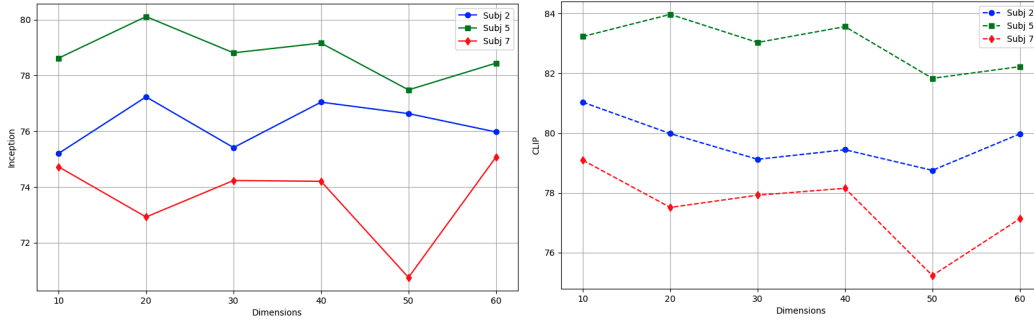


Figure 15. Comparison of the performance of the image selection strategy for different subjects. (a) Inception score with varying number of dimensions (b) CLIP score with varying number of dimensions.

## H.2. Impact of reference subject on performance

We conducted additional experiments (Table 11) to explore the effect of different reference subjects on reconstruction results. We use subjects 2,5 and 7 as the reference and use subject 1 as the fine-tuning subject.

Table 11. Quantitative results on fine tuning a new subject with limited data using different reference subjects. In this table we compare AAMax vs normal finetuning at 160 epochs only since AAMax significantly outperforms normal finetuning after 1 epoch of finetuning.

Method	Low-Level				High-Level			
	PixCorr $\uparrow$	SSIM $\uparrow$	Alex(2) $\uparrow$	Alex(5) $\uparrow$	Incep $\uparrow$	CLIP $\uparrow$	Eff $\downarrow$	SwAV $\downarrow$
Subj1 FT From Subj2 250 Normal E160	0.007	0.268	75.55%	84.00%	75.20%	74.60%	0.862	0.520
Subj1 FT From Subj2 250 AAMAX E160	<b>0.06</b>	<b>0.277</b>	<b>81.13%</b>	<b>88.99%</b>	<b>79.71%</b>	<b>78.89%</b>	<b>0.824</b>	<b>0.494</b>
Subj1 FT From Subj5 250 Normal E160	0.094	0.239	71.54%	80.10%	73.11%	74.02%	0.875	0.537
Subj1 FT From Subj5 250 AAMAX E160	<b>0.105</b>	<b>0.259</b>	<b>76.77%</b>	<b>86.20%</b>	<b>80.08%</b>	<b>80.14%</b>	<b>0.828</b>	<b>0.496</b>
Subj1 FT From Subj7 250 Normal E160	0.010	0.266	74.96%	81.55%	71.71%	73.72%	0.874	0.528
Subj1 FT From Subj7 250 AAMAX E160	<b>0.012</b>	<b>0.283</b>	<b>79.58%</b>	<b>87.78%</b>	<b>77.48%</b>	<b>77.87%</b>	<b>0.835</b>	<b>0.502</b>

## I. High-Level Pipeline Training Process

The high-level pipeline aims to map input fMRI signals to the CLIP embedding space. The training process differs based on whether the subject is the reference subject or a new subject being aligned to the reference space.

### I.1. Training the Reference Subject

For the reference subject, the loss function combines Diffusion Prior Loss and CLIP Loss. The overall loss for the reference subject is:

$$\mathcal{L}_{\text{ref}} = \lambda_1 \mathcal{L}_{\text{Prior}} + \lambda_2 \mathcal{L}_{\text{CLIP}}$$

where  $\lambda_1$  and  $\lambda_2$  are weighting coefficients for the respective loss components.

### I.2. Training a New Subject

For a new subject, the training involves two stages:

**Stage 1: Adapter-Level Alignment.** Initially, the adapter is trained using the Mean Squared Error (MSE) loss:

$$\mathcal{L}_{\text{adapter}} = \mathcal{L}_{\text{MSE}}(\mathbf{z}_{\text{adapter, new}}, \mathbf{z}_{\text{adapter, ref}})$$

where  $\mathbf{z}_{\text{adapter, new}}$  and  $\mathbf{z}_{\text{adapter, ref}}$  are the adapter-level embeddings for the new and reference subjects, respectively, on the shared common images.

**Stage 2: End-to-End Training.** After aligning the adapter, the entire pipeline is trained end-to-end. During this stage:

- For non-common images, Prior Loss and CLIP Loss are applied to align the new subject's output embeddings to the CLIP space.
- For common images, the MSE Loss is applied at the adapter level to retain the alignment to the reference subject as much as possible.

The overall loss function in this stage is:

$$\mathcal{L}_{\text{new}} = \begin{cases} \lambda_1 \mathcal{L}_{\text{Prior}} + \lambda_2 \mathcal{L}_{\text{CLIP}}, & \text{for non-common images} \\ \lambda_1 \mathcal{L}_{\text{Prior}} + \lambda_2 \mathcal{L}_{\text{CLIP}} + \lambda_3 \mathcal{L}_{\text{MSE}}(\mathbf{z}_{\text{new}}, \mathbf{z}_{\text{ref}}), & \text{for common images} \end{cases}$$

where  $\mathbf{z}_{\text{adapter, new}}$  and  $\mathbf{z}_{\text{adapter, ref}}$  are the adapter-level embeddings for the new and reference subjects, respectively, on the shared common images.

## J. Low-Level Pipeline Training Process

The low-level pipeline aims to map input fMRI signals to the latent space of an Autoencoder (AE), which is trained to compress the NSD train images into a 1024-dimensional latent representation and reconstruct them. The training process differs based on whether the subject is the reference subject or a new subject being aligned to the reference space.

### J.1. Training the Reference Subject

For the reference subject, the goal is to map the fMRI signals to the AE latent space using the Mean Squared Error (MSE) loss. The AE latent representations of the corresponding images serve as the ground truth.

The loss function for the reference subject is:

$$\mathcal{L}_{\text{ref}} = \mathcal{L}_{\text{MSE}}(\mathbf{z}_{\text{fMRI}}, \mathbf{z}_{\text{AE}})$$

where  $\mathbf{z}_{\text{fMRI}}$  is the mapped output embedding from fMRI signals, and  $\mathbf{z}_{\text{AE}}$  is the AE latent space representation of the corresponding image.

## J.2. Training a New Subject

For a new subject, the training involves two stages:

**Stage 1: Adapter-Level Alignment.** In this stage, only the adapter is trained using MSE Loss to align the new subject's adapter-level embeddings with those of the reference subject for shared common images:

$$\mathcal{L}_{\text{adapter}} = \mathcal{L}_{\text{MSE}}(\mathbf{z}_{\text{adapter, new}}, \mathbf{z}_{\text{adapter, ref}})$$

where  $\mathbf{z}_{\text{adapter, new}}$  and  $\mathbf{z}_{\text{adapter, ref}}$  are the adapter-level embeddings for the new and reference subjects, respectively.

**Stage 2: End-to-End Training.** In this stage, the entire pipeline is trained end-to-end. MSE Loss is applied at 2 points in the pipeline:

- At the adapter level, to maintain alignment between the new subject's embeddings and the reference subject's embeddings for common images.
- At the mapper output level, to ensure the new subject's fMRI embeddings align with the AE latent representations for corresponding images.

The loss function for this stage is:

$$\mathcal{L}_{\text{new}} = \begin{cases} \mathcal{L}_{\text{MSE}}(\mathbf{z}_{\text{fMRI, new}}, \mathbf{z}_{\text{AE}}), & \text{for non-common images} \\ \mathcal{L}_{\text{MSE}}(\mathbf{z}_{\text{fMRI, new}}, \mathbf{z}_{\text{AE}}) + \mathcal{L}_{\text{MSE}}(\mathbf{z}_{\text{adapter, new}}, \mathbf{z}_{\text{adapter, ref}}), & \text{for common images} \end{cases}$$

where:

- $\mathbf{z}_{\text{fMRI, new}}$ : Output embedding for the new subject.
- $\mathbf{z}_{\text{AE}}$ : AE latent space representation of the image.
- $\mathbf{z}_{\text{adapter, new}}$  and  $\mathbf{z}_{\text{adapter, ref}}$ : Adapter-level embeddings for the new and reference subjects, respectively.

## K. Reconstruction Results

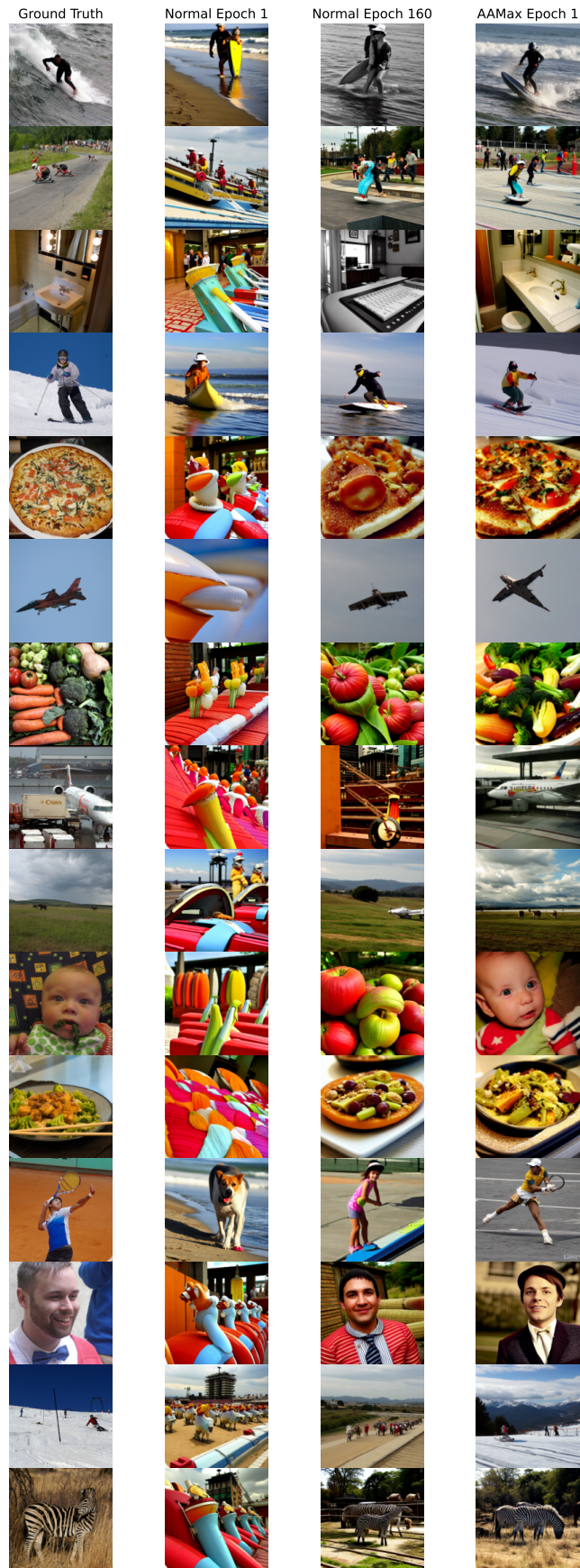


Figure 16. Reconstruction results after fine-tuning on 250 common images